Nano Research

Open Access

Research Article

Upconverted microrobots alleviate the idiopathic pulmonary fibrosis via improving the respiratory depression

Hua Liu[1,§], Kaige Zheng[1,§], Mingzhu Yang[1], Qixiang Zhang[1], Fengqin Zhao[1], Xuejiao Zeng[1], Yanbo Yang[1], Wei Gao[6] ✉, Na Yin[2,5] ✉, Jinjin Shi[1,3,4,5] ✉, and Zhi-Hao Wang[1,3,4,5] ✉

[1] *School of Pharmaceutical Sciences, Zhengzhou University, Zhengzhou 450001, China*
[2] *School of Basic Medical Science, Zhengzhou University, Zhengzhou 450001, China*
[3] *Henan Key Laboratory of Targeting Therapy and Diagnosis for Critical Diseases, Zhengzhou 450001, China*
[4] *State Key Laboratory of Antiviral Drugs, Pingyuan Laboratory, Zhengzhou University, Zhengzhou 450001, China*
[5] *Tianjian Laboratory of Advanced Biomedical Sciences, Zhengzhou University, Zhengzhou 450001, China*
[6] *School of Electronic Engineering, Xian University of Posts & Telecommunications, Xi'an 710121, China*
§ *Hua Liu and Kaige Zheng contributed equally to this work.*

Cite this article: *Nano Research*, **2026**, *19*, 94908538. https://doi.org/10.26599/NR.2026.94908538

ABSTRACT: Idiopathic pulmonary fibrosis (IPF) is a chronic and progressive pulmonary disorder characterized by fibrotic scarring, hypoxemia, and dyspnea. Although oxygen therapy is widely used to relieve acute dyspnea, it faces limitations such as oxygen toxicity and patient immobility. To address these challenges, this study developed upconversion-based microrobots capable of mitigating IPF through *in situ* oxygen generation. These microrobots consist of *Chlamydomonas reinhardtii* algae functionalized with upconversion nanoparticles. Upon inhalation and exposure to near-infrared light, the microrobots convert the incident light into red visible light, driving photosynthetic oxygen production at a rate of 0.298 ± 0.005 mg·(L·min)$^{-1}$. Moreover, their autonomous mobility within the mucus enhances the uniformity of oxygen distribution and prolongs retention by evading pulmonary macrophage clearance. In a murine model of IPF, the microrobots effectively alleviated hypoxia, as evidenced by reduced hypoxia-inducible factor 1-alpha (HIF-1*α*) expression in fibrotic lung tissues and elevated blood oxygen saturation. This platform presents an efficient and promising strategy for oxygen therapy in IPF and broader pulmonary oxygen-dependent applications.

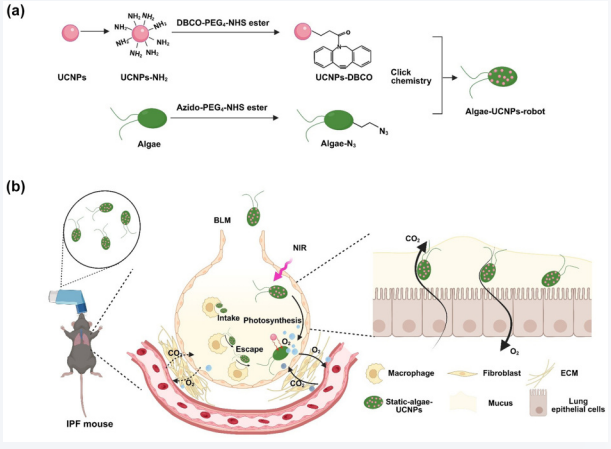

KEYWORDS: idiopathic pulmonary fibrosis, hypoxia, microalgae robot, photosynthesis, macrophage

1 Introduction

Idiopathic pulmonary fibrosis (IPF) is a chronic, progressive, and irreversible fibrotic interstitial lung disease of unknown etiology [1, 2]. The median survival time for most patients is typically 3–5 years [3, 4]. As the disease progresses, significant decline in lung function and severe hypoxemia can lead to persistent dyspnea [5, 6]. Even at rest, the patients may experience severe shortness of breath and be unable to engage in physical activity. Currently, Pirfenidone and Nintedanib are the only two U. S. Food and Drug Administration (FDA)-approved antifibrotic drugs for the IPF treatment [7, 8]. However, clinical evidence suggests that these medications only slow disease progression and do not provide immediate relief from acute dyspnea [9, 10]. For patients experiencing dyspnea, symptomatic management typically involves a combination of oxygen therapy, pulmonary rehabilitation, and anti-inflammatory treatments [11]. Studies indicate that long-term high-concentration oxygen therapy via ventilators may cause oxygen toxicity and induce lung injury [12], and oxygen therapy requires patients to continuously wear oxygen equipment [13],

Received: November 4, 2025; **Revised:** February 3, 2026
Accepted: February 4, 2026

✉Address correspondence to Wei Gao, gaowei@xupt.edu.cn; Na Yin, yinna@zzu.edu.cn; Jinjin Shi, shijinyxy@zzu.edu.cn; Zhi-Hao Wang, wangzhihao@zzu.edu.cn

which limits daily activities and quality of life. Therefore, there is an urgent need to develop safer and more convenient oxygen delivery methods.

To address these challenges, researchers have investigated a range of novel oxygen delivery strategies, such as hyperbaric oxygen therapy (HBOT) [14], oxygen-carrying nanomaterials [15], perfluorocarbon-based oxygen carriers [16, 17], biomimetic red blood cell oxygen carriers [18, 19], and nanozyme-catalyzed oxygen generation [20]. However, these approaches still face significant challenges concerning biosafety, oxygen delivery efficiency, and distribution uniformity [21, 22]. Consequently, the development of safer and more efficient oxygen delivery systems has emerged as a critical research priority. In nature, microalgae, capable of oxygen production via photosynthesis, are regarded as one of the planet's most vital "oxygen factories" [23], and exhibit good biocompatibility [24]. For instance, an oxygen-generating device incorporating Chlorella within a hydrogel matrix has been demonstrated to produce 151 mL of oxygen continuously for over 60 days [25]. In a representative application, Chlorella encapsulated by erythrocyte membranes was delivered to tumor tissue. The subsequent red light-induced *in situ* oxygen generation significantly alleviated intratumoral hypoxia, leading to a marked enhancement of radiotherapy efficacy [26]. However, these non-motile microalgae mainly depend on passive diffusion for oxygen delivery, which may restrict oxygen transport and distribution in the structurally complex pulmonary environment. Therefore, microalgae with intrinsic motility may offer advantages for improving local oxygen dispersion in lung tissue. Otherwise, lasers with wavelengths below 585 nm exhibit limited tissue penetration, typically reaching depths of only 2–4 mm beneath the epidermis, which is insufficient for accessing most subcutaneous targets. Consequently, longer-wavelength irradiation is essential for *in vivo* applications such as drug delivery [27]. Although the 980 nm laser has excellent tissue penetration, it cannot be used directly for photosynthesis. Upconversion nanoparticles (UCNPs), which possess the unique capability of converting long-wavelength light into shorter-wavelength visible light, can bridge this gap. For instance, upon 980 nm laser irradiation, cyanobacteria hybridized with UCNPs have been shown to perform photosynthesis *in vivo* [28, 29]. Therefore, the integration of near-infrared (NIR) light with UCNPs represents a promising strategy to achieve efficient *in vivo* photosynthesis.

Chlamydomonas reinhardtii (C. reinhardtii) is a single-celled microalgae that produce O_2 through photosynthesis [30]. They are easy to culture, have advantages such as self-fluorescence, photochemotaxis. Most importantly, there are two equally long flagella at the front of the algae cell, and the flagella-based beat can propel the algae cells forward at speeds of up to 110 $\mu m \cdot s^{-1}$ [31, 32]. At present, *C. reinhardtii*-based microrobots have attracted wide attention, and their efficient movement properties offer significant benefits for the treatment of lung diseases, such as rapid dispersion and and distribution throughout the pulmonary tract, prolonged retention time, and demonstrated efficacy against bacterial pneumonia [33, 34]. We developed a bioinspired microrobotic platform, the Algae-UCNPs-robot, by conjugating amino-functionalized UCNPs (UCNPs-NH_2) onto the surface of *C. reinhardtii*. This platform is designed to alleviate hypoxia in the lungs of mice with idiopathic pulmonary fibrosis through *in vivo* O_2 generation (Scheme 1). Under NIR laser irradiation at 980 nm, UCNPs could effectively convert the incident laser into a red (642–681 nm) emission band. The upconverted red luminescence is suitable for inducing algae cells to produce oxygen through photosynthesis [26]. The experimental results showed that, compared to *C. reinhardtii* without UCNPs, the O_2 production efficiency of the microalgae robots under NIR light irradiation was 2.4 times higher. Additionally, microalgae robots, with their

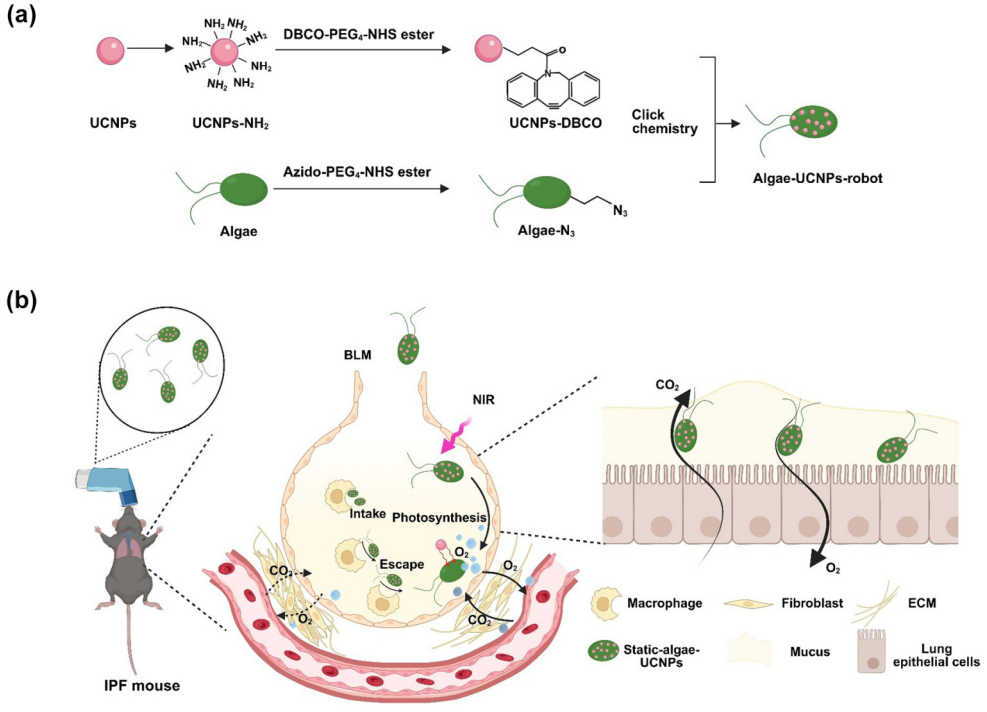

Scheme 1 (a) Schematic diagram of the preparation process of Algae-UCNPs-robot. (b) Schematic diagram of relieving lung hypoxia in mice with IPF by atomizing Algae-UCNPs-robot.

mobility, were able to evade phagocytosis by alveolar macrophages, prolonging their retention time in the lungs and enabling more uniform distribution of O_2. This process reduced the expression of hypoxia-inducible factor 1-alpha (HIF-1α) in hypoxic lung tissue by approximately 50%. These effects significantly improved tissue oxygenation, alleviated hypoxia in the lungs of IPF mice, slowed disease progression, and markedly improved their symptoms of dyspnea.

2 Experimental

2.1 Materials and green algae culture

Azido (N_3)-PEG$_4$-NHS ester and DBCO-PEG$_4$-NHS ester were purchased from Aladdin Biochemical Technology Co., Ltd (Shanghai, China). SYTOX Green nucleic acid dye was purchased from Thermo Fisher Scientific Ltd (Waltham, USA). Boron-dipyrromethene-fluorescent-dibenzocyclooctyne (BDP-FL-DBCO) was purchased from KKL Biomedical Co., Ltd (Beijing, China). Mucin from porcine gastrointestinal tract and bleomycin (BLM) were purchased from Yuanye Bio-Technology Co., Ltd (Shanghai, China). HIF-1α monoclonal antibody, goat anti-mouse IgG-AF488 antibody, fluorescein isothiocyanate (FITC) CD11b$^+$ antibody, and PE F4/80$^+$ antibody were purchased from absin Biotechnology Co., Ltd (Shanghai, China). Green *C. reinhardtii* algae (strain CC-125 wild-type mt+) were purchased from Freshwater Algae Culture Collection at the Institute of Hydrobiology (FACHB), Chinese Academy of Sciences (CAS). The algae were transferred from the agarose (AGAR) plate to the tris-acetate-phosphate (TAP) medium (Leading Tec), with alternating cycles of 12 h of daylight and 12 h of darkness at room temperature (about 25 °C).

2.2 Cells and animals

A549 cells (human lung adenocarcinoma cells; RRID: CVCL_0023) were purchased from the cell bank of Chinese Academy of Science (Shanghai, China). RAW264.7 cells (mouse mononuclear macrophage leukemia cells; RRID: CVCL_0493) were purchased from Pricella Biotechnology Co., Ltd (Wuhan, China). A549 cells were cultured using RPMI-1640 medium mixed with 15% fetal bovine serum (FBS, Servicebio, China), and RAW264.7 cells were cultured using RAW complete medium (Procell, China). All experimental procedures involving animals strictly abide by the Regulations on the Management of Experimental Animals of Zhengzhou University and have been approved by the Life Science Ethics Review Committee of Zhengzhou University (animal ethics code: yxy11sc20250012). Male C57BL/6 mice (6–8 weeks) were purchased from Liaoning Changsheng Biotechnology Co. Ltd (SCXK-2020-0001).

2.3 Description of the synthesis of UCNPs

The oil-soluble UCNPs were provided by the research group of Professor Wei Gao from Xi'an University of Posts and Telecommunications. Core-shell UCNPs ($NaErF_4$) were synthesized via high-temperature co-precipitation: The oil-soluble UCNPs were synthesized via high-temperature co-precipitation. For $NaErF_4$ core-shell UCNPs, erbium chloride ($ErCl_3{\cdot}6H_2O$), octadecene (ODE), and oleic acid (OA) were reacted at 160 °C for 1 h. After cooling, NaOH and NH_4F in methanol were added, followed by further reaction and heating to 300 °C under argon. The product was washed and dispersed in cyclohexane. Similar steps were used for $NaErF_4$:Tm^{3+} and $NaErF_4$:Tm^{3+}@$NaYF_4$. For water dispersion, oleate ligands on UCNPs were exchanged with alendronic acid (ADA) by stirring in a mixed solvent (cyclohexane/ethanol/water) at pH 2–3. The resulting UCNPs-NH_2 were centrifuged and dispersed in water.

2.4 Preparation of Algae-UCNPs-robot

The algae were washed three times with PBS (pH 7.4), centrifuged at 2000 rpm for 5 min, and adjusted to a concentration of 1×10^7 cells·mL^{-1} before resuspension in PBS. N_3-PEG$_4$-NHS ester (40 μM, click chemistry reagent) was added and incubated at room temperature for 1 h to introduce N_3 groups onto the surface of *C. reinhardtii*. To verify successful modification, the algae were incubated with borodipyrromethane FL DBCO (KKL, China) for 30 min and imaged by confocal laser scanning microscopy (CLSM). UCNPs were functionalized with 40 μM DBCO-PEG$_4$-NHS ester (click chemistry reagent) for 1 h. The modified algae and UCNPs were then mixed and incubated for 45 min, followed by centrifugation and washing to obtain the Algae-UCNPs-robot, which were resuspended in TAP medium. Static-algae-UCNPs were prepared by removing flagella with 0.5 M acetic acid prior to UCNP conjugation.

2.5 Algae viability study

To assess algae viability, the algae were stained with 5 μM SYTOX Green (Thermo Fisher, USA). The bright green fluorescence of dead algae was observed by CLSM, and the cell viability of algae was calculated by counting.

2.6 UCNPs binding optimization

To optimize the binding efficiency, we used different concentrations of UCNPs, specifically 0.2, 0.5, 1.0, and 2.0 mg·mL^{-1}, for conjugation. First, UCNPs (2.0 mg·mL^{-1}) were incubated with DBCO-PEG$_4$-NHS ester, FITC solution was added overnight. Then, the concentration of FITC-UCNPs was diluted to 1.0000, 0.5000, 0.2000, 0.1250, and 0.0625 mg·mL^{-1}, and the fluorescence intensity of each diluent was determined and the standard curve was established. Different concentrations of FITC-UCNPs were incubated with algae, the unreacted UCNPs were removed by centrifugation and the fluorescence intensity was measured to determine the binding amount of the UCNPs.

2.7 Characterization of Algae-UCNPs-robot

In order to perform scanning electron microscopy (SEM) characterization, Algae-UCNPs-robots were first fixed in 2.5% glutaraldehyde overnight and then dried at critical point after gradient dehydration with ethanol. After drying for about 1 h, gold spraying was performed on Algae-UCNPs-robots. The SEM instrument (SU8020 Hitachi) with 5 kV acceleration voltage was used for scanning electron microscopy characterization. In addition, UCNPs were labeled with FITC, the self-luminescence (645–664 nm) of green algae and fluorescence of UCNPs in the Algae-UCNPs-robots were detected by CLSM. The attachment of UCNPs to algae was successfully captured.

2.8 Optical video recording and MSD analysis

In order to explore the effect of nanoparticles modification on the movement speed of *C. reinhardtii*, the movement velocity of algae modified with different bindings of nanoparticles was measured in TAP medium. In addition, the movement of Algae-UCNPs-robot

in mucin solution was evaluated. The motion velocities of bare algae and Algae-UCNPs-robot were measured in the dark at 37 °C and evaluated at 0.5, 1, 2, 12, and 24 h. The motion of algae-nanorobots was imaged by using the bright field of fluorescence microscope (Nikon ECLIPSE Ji) and the mean-squared displacement (MSD) was calculated (Eq. (1), $i = 2$ for 2D analysis).

$$\mathrm{MSD}(\Delta t) = [x_i(t+\Delta t) - x_i(t)]^2 \quad (1)$$

where $x_i(t)$ represents the coordinate of the nanosystem at time t, $x_i(t + \Delta t)$ represents the coordinate of the nanosystem at time $t + \Delta t$, Δt represents the time interval, and t stands for time.

2.9 O_2 production of Algae-UCNPs-robot

Green algae (1×10^7 cells·mL^{-1}) were incubated with UCNPs of different concentrations (0.2, 0.5, 1.0, and 2.0 mg·mL^{-1}) and then re-suspended in PBS (pH 7.4) with a final concentration of 5×10^6 cells·mL^{-1} (total volume: 10 mL). The algae were placed in the dark for 1 h and irradiated with NIR laser at a distance of 10 cm for 600 s. A portable dissolved oxygen meter (JPB-607A) was used to record the oxygen concentration at intervals, so as to evaluate the oxygen production of green algae after modification with different concentrations of UCNPs. In addition, in order to assess the oxygen production of Algae-UCNPs-robot in mucin solution, the Algae-UCNPs-robot were placed in 2% mucin solution with the same final concentration and volume as above, placed in the dark for 1 h, irradiated with NIR laser for 600 s, and recorded oxygen concentration by portable dissolved oxygen meter.

2.10 *In vitro* cell oxygenation by $Ru(dpp)_3Cl_2$ probe

A549 cells were uniformly inoculated into 24-well plates with a cell density of 5×10^4 cells per well for 12 h, and then the 24-well plates were placed into anaerobic bags (Anaero Pack) for anaerobic culture, leaving A549 cells in anoxic state. 10 μg·mL^{-1} $[Ru(dpp)_3]Cl_2$ (RDPP) RPMI-1640 medium was added, cultured for 3 h, followed by two quick washes with PBS. Subsequently, 1 mL of RPMI-1640 medium containing UCNPs, Algae, or Algae-UCNPs-robot was added to respective wells. Among them, the ratio of algae and Algae-UCNPs-robots to A549 cells was 64:1. After culturing under closed conditions for 3 h, it was irradiated with NIR laser for 10 min. After twice rinsing of the medium, fluorescence was observed by CLSM photography (excitation: 455 nm, emission: 613 nm).

2.11 HIF-1*α* protein quantification

To verify the oxygen production of Algae-UCNPs-robot under NIR irradiation at the cellular level, the characterization was performed by detection of HIF-1*α*. A549 cells were cultured in a cell culture dish for 12 h, and the dish was placed in an anaerobic bag to keep A549 cells in a hypoxic state. 1 mL of 1640 suspended UCNPs, Algae and Algae-UCNPs-robot were added respectively, cultured in closed condition for 3 h, and irradiated in closed condition with NIR laser for 10 min. Then, the liquid in the dish was removed, the lysis buffer was quickly added, and shake on the ice for 30 min. The cracked cells were quickly scraped with a cell scraper, centrifuged at 12,000 rpm, 4 °C, for 15 min, and the supernatant was taken for subsequent western blot analysis (WB) test.

2.12 *In vitro* cytotoxicity assay

A549 cells were seeded in 96-well plates at 1×10^4 cells/well and cultured for 12 h. After washing with PBS, cells were treated with algae or Algae-UCNPs-robot at various algae-to-cell ratios (0.0625–32) for 3 h, followed by NIR irradiation (10 min). After 24 h incubation, cell viability was assessed using the cell counting kit-8 (CCK-8) assay. RAW264.7 cells were evaluated under identical conditions.

2.13 *In vitro* macrophage phagocytosis

RAW 264.7 macrophages were cultured in 24-well plates with a density of 1×10^6 cells per well. Then the Algae-UCNPs-robots were added in a 1:1 ratio of robot/RAW264.7 macrophages and incubated at 37 °C. The mixture was analyzed by fluorescence microscopy at specific time points 0, 2, 8, 12, 24, and 48 h, and the fluorescence values were quantified by microplate reader (Thermo Fisher Scientific).

2.14 *In vivo* macrophage phagocytosis

Male C57BL/6 mice were nebulized with Algae-UCNPs-robot or Static-algae-UCNPs. The robot group received NIR irradiation (980 nm, 1.5 W·cm^{-2}, 10 min) post-nebulization. At different time points (1, 6, and 24 h) intervals, BALF was collected after euthanasia. Red blood cells were lysed, and macrophages were stained with FITC-CD11b$^+$/PE-F4/80$^+$ antibodies (4 °C, 30 min). Flow cytometry (FlowJo analysis) quantified macrophage uptake of the robots.

2.15 Establishment of animal model

Mice were anesthetized with intraperitoneal pentobarbital sodium (50 mg·kg^{-1}). A 1 cm midline neck incision was made to expose the trachea, followed by intratracheal injection of 50 μL bleomycin (2 U·kg^{-1} in saline). The mice were then rotated horizontally to ensure even lung distribution. Control mice received an equal volume of saline. Bleomycin (Shanghai Green Leaf Co., Ltd., Cat# S17100) was used to induce pulmonary fibrosis.

2.16 *In vitro* lung imaging

Mice were atomized by Static-algae-UCNPs and Algae-UCNPs-robot at the same concentration (5×10^6 cells·mL^{-1}). After the specific time point (1, 3, 6, 12, 24, and 48 h), each group of mice was sacrificed, and their lungs were collected for analysis. Isolated lung images were taken with Lumina XRMS *in vivo* imaging system. Finally, the fluorescence was semi-quantified by ImageJ (4.3.1) software.

2.17 Metabolism of UCNPs *in vivo*

DBCO-PEG_4-NHS ester-modified UCNPs were labeled with FITC and incubated with algae for 45 min to prepare Algae-UCNPs-robots (final concentration: 5×10^6 cells·mL^{-1}). Following nebulization administration, mice were sacrificed at 3, 6, 9, 12, 24, and 48-h time points. Blood, lung tissue, and other major organs were collected for nanoparticle metabolism analysis using inductively coupled plasma mass spectrometry (ICP-MS) and *in vivo* imaging system (Lumina XRMS).

2.18 *In vivo* administration scheme

This study established an IPF mouse model via intratracheal BLM injection, with successful model validation by hematoxylin and eosin (H&E) staining on day 7 post-modeling. Mice were randomly divided into seven groups (n = 5/group): (1) Healthy Control; (2) Model Control; (3) SAL group (5 mg·mL^{-1} salbutamol, SAL, daily nebulization); (4) Algae + NIR group; (5) Algae-UCNPs-

robot + dark group; (6) Static-algae-UCNPs + NIR group; and (7) Algae-UCNPs-robot + NIR group (the last four groups administered at 5×10^6 cells·mL^{-1}, 500 μL). Starting from day 1 post-modeling, nebulized treatments were administered on odd-numbered days (days 1, 3, 5, 7, 9, 11, and 13). For NIR groups (1.5 W·cm^{-2}), NIR irradiation was performed for 10 min at 1 h post-nebulization and repeated at the same time point the following day. During the entire atomization process, the body weight of each mouse was measured using an electronic balance at fixed intervals every other day, and the weight change curves of each group of mice were plotted. The changes of various pulmonary function parameters of mice were recorded using the small animal non-invasive pulmonary function respiratory detection system at the end of the treatment. Lung tissues were collected for pathological analysis.

2.19 Monitoring SpO_2 and respiratory metabolism in mice

The mice in each group were atomized. One hour after atomization, NIR (1.5 W·cm^{-2}) was used to irradiate the lungs of the mice for 10 min. Subsequently, when the mice were in a stable state, the blood oxygen saturation of the mice was detected using an oximeter. Subsequently, the mice were placed in the small animal Respiratory Metabolism Detection System (Tarvim Tech) to monitor the changes of the volume of carbon dioxide produced per minute (VCO_2) and the volume of oxygen consumed per minute (VO_2) in the mice.

2.20 *In vivo* safety studies

Mice (n = 3 per group) were randomly assigned to control, Algae-UCNPs-robot, and Algae-UCNPs-robot + NIR groups for a two-week nebulization study. After the end of administration, blood was taken from the orbit of the mice, and the organs (heart, liver, spleen, lung and kidney) of the mice in each group were dissected, rinsed thoroughly with normal saline and fixed with 4% paraformaldehyde fixative solution. Then the cured tissues were cut into thin slices, stained with H&E, and photographed with a slide scanner. Mouse whole blood was collected into heparin-containing Eppendorf (EP) tubes and centrifuged at 3000 rpm for 20 min at 4 °C to obtain serum. The levels of interleukin-6 (IL-6) and tumor necrosis factor-α (TNF-α) in the supernatant were then quantified using assay kits (Shanghai DuMa Biotechnology Co.Ltd.).

2.21 Statistical analysis

Statistical analysis between groups was analyzed by GraphPad Prism 6.0 software with analysis of variance (ANOVA). All data with error bars in this study are presented as the mean ± standard deviation (SD) of at least three independent experiments. $^*P < 0.05$ indicates a statistically significant difference; $^{**}P < 0.01$ indicates a highly statistically significant difference; $^{***}P < 0.001$ indicates an extremely statistically significant difference.

3 Results and discussion

3.1 Preparation and characterization of Algae-UCNPs-robot

To evaluate the impact of UCNPs with distinct emission wavelengths on the oxygen production of *C. reinhardtii*, three types of UCNPs—UCNPs-$NaYF_4$:20%Yb,2%Er@$NaYF_4$ (green emission), $NaYF_4$:2%Er@$NaYF_4$ (yellow emission), and $NaErF_4$:0.5%Tm@$NaYF_4$ (red emission)—were synthesized via an argon-protected pyrolysis method. These UCNPs were separately mixed with *C. reinhardtii* cultures and irradiated under NIR light for 10 min. The oxygen yield in the red-emitting UCNPs group reached 2.92 ± 0.26 mg·L^{-1}, which was 2.89 and 2.33 times higher than that of the green- and yellow-emitting groups, respectively (Fig. S1 in the Electronic Supplementary Material (ESM)). Given its superior performance in enhancing oxygen production, $NaErF_4$:0.5%Tm@$NaYF_4$ was selected for the subsequent fabrication of microalgae-based robots. Transmission electron microscopy (TEM) characterization revealed that the as-synthesized UCNPs exhibit a uniform short-rod morphology, with an average particle size of 43.99 ± 0.81 nm (Fig. S2 in the ESM).

To improve the dispersion of UCNPs in aqueous solution, we performed a surface amination via a ligand exchange process. TEM images confirmed that the aminated UCNPs maintained a uniform rod-like morphology with an average particle size of 47.99 ± 2.37 nm (Figs. 1(a) and 1(b)). X-ray diffraction (XRD) patterns further verified that both the original and aminated UCNPs retained a pure hexagonal phase (JCPDS: 27-068), indicating that the surface modification did not alter the crystal structure (Fig. 1(c)). Successful ligand exchange was corroborated by fourier transform infrared spectroscopy (FTIR). The appearance of a characteristic peak at 1056 cm^{-1}, attributed to the P–O stretching vibration of the ADA ligands, alongside the significant suppression of the characteristic C–H stretching (2920 and 2850 cm^{-1}) and bending (1465 cm^{-1}) vibrations of OA, collectively confirms the successful amination of the UCNPs (Fig. S3 in the ESM).

To prepare Algae-UCNPs-robot, we cultured *C. reinhardtii* algae in TAP medium. Ultraviolet–visible (UV–Vis) spectroscopy showed that *C. reinhardtii* had a characteristic absorption peak at 680 nm (Fig. S4(a) in the ESM) and was in a good growth state (Fig. S4(b) in the ESM). To facilitate the determination of the quantity of *C. reinhardtii*, the relationship between the number of *C. reinhardtii* and OD680 was established, and a linear curve was plotted (Fig. S4(c) in the ESM). To further modify the microalgae, we successfully conjugated N_3-PEG_4-NHS ester to microalgae using an amide bond formation reaction between primary amines on the surface of the algae and esters, and observed negligible cytotoxicity of N_3-PEG_4-NHS ester (Fig. S5 in the ESM).

To assemble the Algae-UCNPs-robot, the N_3-modified algae were conjugated with DBCO-functionalized UCNPs via a bioorthogonal click reaction (Fig. 1(d)). SEM and CLSM analyses visually confirmed the successful assembly of the Algae-UCNPs-robot. SEM images directly showed that UCNPs attached to the surface of N_3-modified *C. reinhardtii* (Figs. 1(e) and 1(f), and Fig. S6 in the ESM), while CLSM revealed clear co-localization of green fluorescence from FITC-labeled UCNPs and red autofluorescence from *C. reinhardtii* chlorophyll a (Fig. 1(g)). Zeta potential analysis provided supplementary evidence for the successful assembly of hybrid robots. Native *C. reinhardtii* exhibited a negative surface charge (−11.92 ± 2.43 mV) due to membrane components such as phospholipids and glycolipids, whereas UCNPs-NH_2 displayed a positive charge (18.45 ± 1.21 mV) attributable to their surface amine groups. Following conjugation, the hybrid robots showed an intermediate zeta potential (−6.02 ± 2.65 mV), confirming effective coverage of the algae surface by the positively charged nanoparticles (Fig. 1(h)). Quantitative analysis of UCNPs loading revealed a concentration-dependent increase in the amount of UCNPs bound

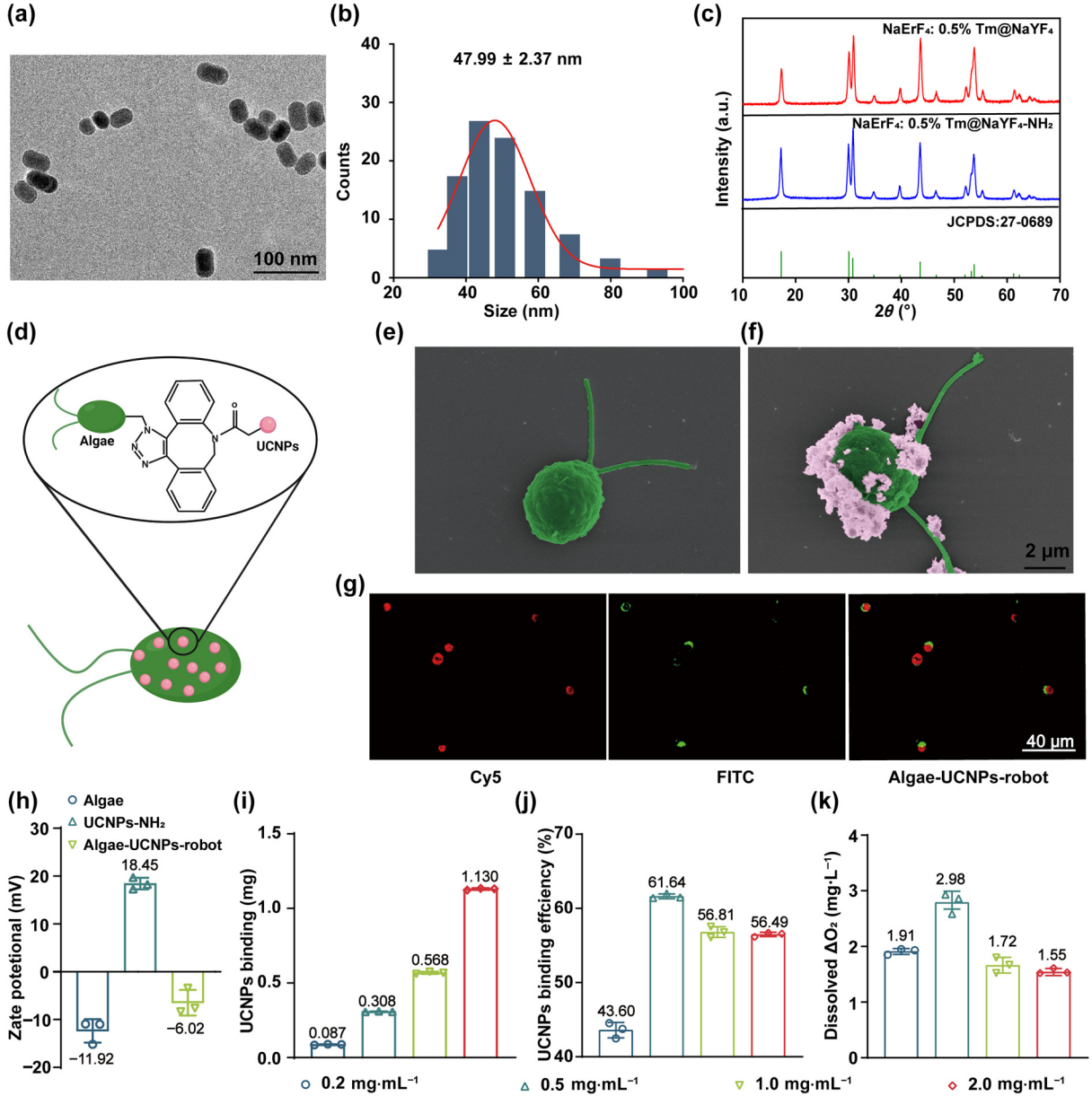

Figure 1 Preparation and structural characterization of Algae-UCNPs-robot. (a) TEM images and (b) particle size distribution of UCNPs-NH_2. (c) XRD pattern of UCNPs before and after amination. (d) Schematic of the functionalization of *C. reinhardtii* with amino UCNPs using click chemistry. Pseudo-coloured SEM images of (e) unmodified algae and (f) Algae-UCNPs-robot (n = 3). (g) CLSM image of red fluorescence of chlorophyll a in *C. reinhardtii* co-located with green fluorescence of FITC produced by UCNPs (n = 3). (h) Potential changes in the synthesis of Algae-UCNPs-robot (n = 3). (i) UCNPs binding and (j) binding efficiency on the surface of *C. reinhardtii* modified with different concentrations of UCNPs. (k) Oxygen production of *C. reinhardtii* modified with different concentrations of UCNPs under NIR irradiation for 10 min (n = 3). Values are represented as means ± SD.

to algae as the nanoparticle concentration in the conjugation system increased, which was consistent with expectations (Figs. 1(i) and 1(j)). At an input of 0.5 mg of UCNPs, the binding capacity and efficiency reached 0.308 ± 0.002 mg and 61.64% ± 0.32%, respectively. The optimal oxygen evolution (2.98 ± 0.05 mg·L^{-1}) was achieved at a UCNPs concentration of 0.5 mg·mL^{-1}. However, a further increase in nanoparticle loading led to a significant decline in oxygen output, with yields dropping to 1.72 ± 0.06 mg·L^{-1} (1.0 mg·mL^{-1}) and 1.55 ± 0.04 mg·L^{-1} (2.0 mg·mL^{-1}) (Fig. 1(k) and Fig. S7 in the ESM). Consequently, the 0.5 mg·mL^{-1} concentration, which yielded the highest oxygen production, was selected for all subsequent robot fabrication.

3.2 Motion behavior of Algae-UCNPs-robot

To further optimize the nanoparticle concentration, we evaluated the motility of the microalgae-based robots functionalized with varying amounts of UCNPs. As in Fig. 2(a), the bare microalgae exhibited a velocity of 101.32 ± 12.09 μm·s^{-1} in TAP medium at room temperature (Video S1 in the ESM). Upon functionalization with UCNPs at a concentration of 0.5 mg·mL^{-1}, the velocity of the Algae-UCNPs-robot decreased to 80.85 ± 13.48 μm·s^{-1}. A further increase in UCNPs loading to 1.0 mg·mL^{-1} resulted in a more pronounced reduction in speed, to 46.77 ± 10.56 μm·s^{-1} (Video S2 in the ESM). Correspondingly, the MSD of the robots showed a significant decrease with increasing nanoparticle coverage (Fig. 2(b)).

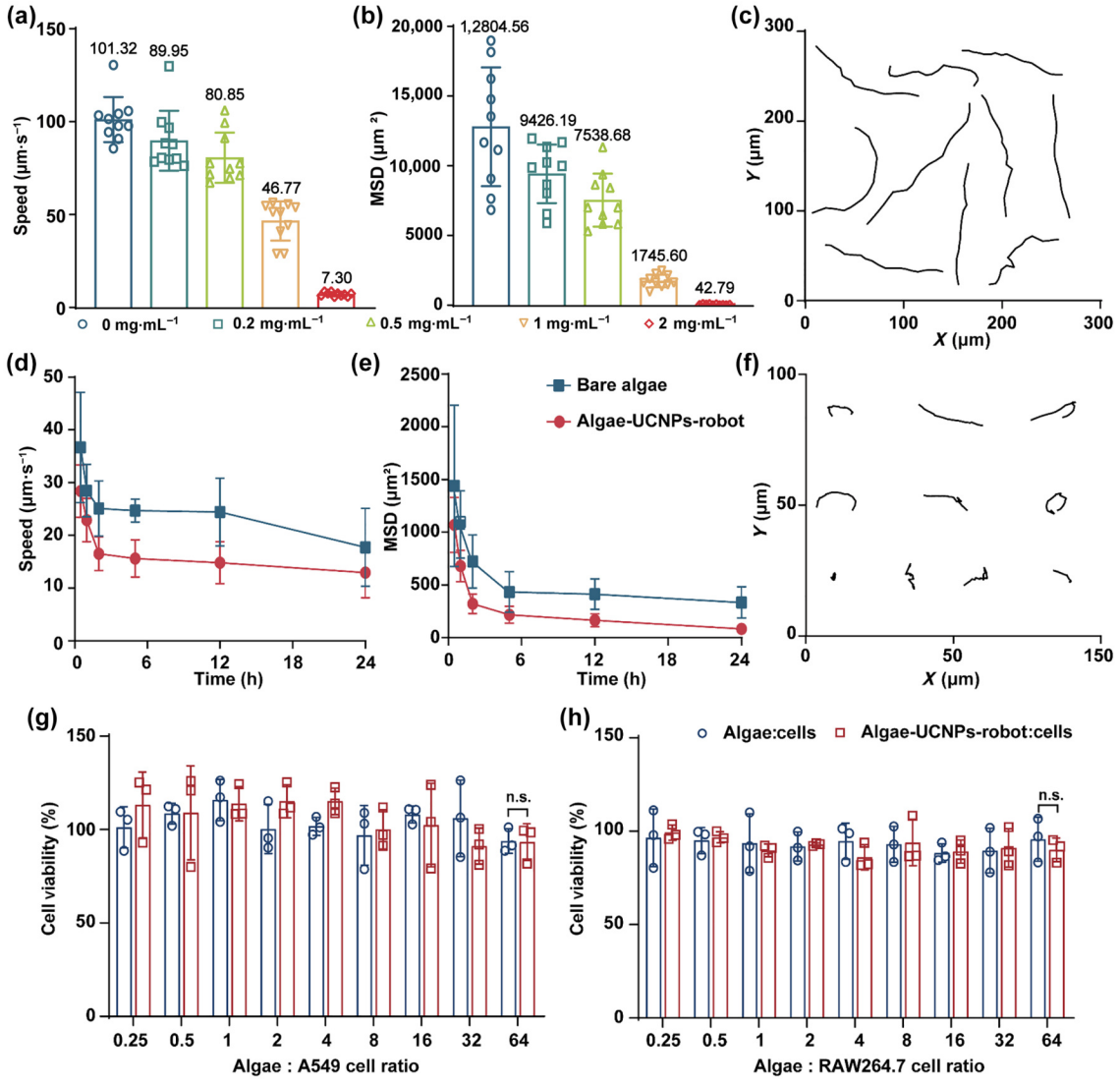

Figure 2 Motion behavior of Algae-UCNPs-robot. After modification with different concentration of nanoparticles, (a) speed, (b) MSD value, and (c) trajectory analysis of Algae-UCNPs-robot within 2 s (n = 10). (d) Motion velocity and (e) MSD value in mucin solution of bare algae and microalgae robot within 2 s. (f) Motion trajectory analysis of mucin suspension of Algae-UCNPs-robot within 2 s after incubation at 37 °C for 24 h (n = 10). (g) Cell viability of A549 human lung epithelial cells and (h) RAW264.7 macrophages incubated with different concentrations of Algae or Algae-UCNPs-robot for 24 h (n = 3). Values are represented as means ± SD. Student's t-test (panels (g) and (h)) was used for statistical analysis. n.s. indicates no significant difference.

This trend in impaired mobility was further corroborated by analyzing the representative motion trajectories of robots with different UCNPs loadings (Fig. 2(c) and Fig. S8 in the ESM). These results collectively demonstrate that the motility of the microalgae is inversely correlated with the UCNPs loading. Therefore, considering both the oxygen production capacity and the motion performance, a UCNPs concentration of 0.5 mg·mL^{-1} was identified as the optimal condition and employed for all subsequent experiments.

The mucus barrier significantly impedes the mobility of micro-nano delivery systems, leading to poor tissue permeability and low bioavailability. To assess the potential of Algae-UCNPs-robot for deep lung delivery, we systematically evaluated their locomotor capability in a mucin-based environment. Bare algae and Algae-UCNPs-robot were dispersed in a mucin solution (prepared with TAP medium), and their locomotion was tracked over time using fluorescence microscopy. As depicted in Fig. 2(d), both systems maintained persistent movement in mucin for up to 24 h at 37 °C (Videos S3 and S4 in the ESM). Quantitative analysis revealed that the velocity of bare algae dropped from 36.69 ± 10.46 μm·s^{-1} (0.5 h) to 17.73 ± 7.40 μm·s^{-1} (24 h), whereas that of the robot decreased from 28.39 ± 4.98 to 12.93 ± 4.82 μm·s^{-1} (Fig. 2(e)). Correspondingly, the MSD values for both systems gradually declined over the 24-h period. Furthermore, analysis of representative trajectories at 2 and 24 h (Fig. 2(f) and Fig. S9 in the ESM) revealed that even after 24 h of incubation, both bare algae and Algae-UCNPs-robot maintained slow but detectable movement in the mucin solution. Together, these data confirm that the Algae-UCNPs-robot maintains sustained mobility in viscous media for at least 24 h. Moreover, both the native algae and the robot showed excellent biosafety profiles: even at a robot-to-cell ratio of 64:1 followed by 10 min of NIR irradiation, A549 and RAW264.7 cells maintained high viability (Figs. 2(g) and 2(h)). This robust cellular biocompatibility supports their potential for *in vivo*

use. Overall, these results indicated that the algae, after being modified with UCNPs, still possessed intrinsic motility behavior, thereby enabling the Algae-UCNPs-robot to be used as an active delivery platform under physiological conditions.

3.3 Oxygen production ability of Algae-UCNPs-robot

The oxygen production capability of the Algae-UCNPs-robot was first evaluated by examining the luminescence spectra of the core material, $NaErF_4$:0.5%Tm@$NaYF_4$. Both before and after the amination process, the samples exhibited distinct emission bands in the green (530–550 nm) and red (640–675 nm) spectral regions. Spectral analysis indicated that the weaker green emission originated from the ($^2H_{11/2}$, $^4S_{3/2}$) → $^4I_{15/2}$ → $^4I_{15/2}$ energy transitions of Er^{3+} ions, while the stronger red emission corresponded to the $^4F_{9/2}$ → $^4I_{15/2}$ transition (Fig. 3(a)). A schematic diagram illustrating this energy transition mechanism is provided in Fig. S10 in the ESM. Furthermore, the upconversion (UC) emission intensity of the UCNPs was notably enhanced following the amination process. This observation suggests that the amination treatment passivates surface defects, thereby improving the luminescence efficiency of the particles [35]. For the Algae-UCNPs-robot complex, the main red upconversion emission peak located at 640–675 nm showed no significant change in either peak position or emission intensity compared to the nanoparticles. This observation directly confirmed that conjugation with algae does not compromise the core upconversion luminescence properties of the nanoparticles, thereby ensuring their reliability as optical reporter units.

To systematically investigate the influence of NIR power density on the oxygen production of the microrobots, we measured the oxygen generated by the Algae-UCNPs-robot over 600 s under NIR irradiation at power densities of 0, 0.5, 1.0, 1.5, and 2.0 W·cm^{-2} using a dissolved oxygen meter. The results indicated that the highest oxygen yield of 2.95 ± 0.17 mg·L^{-1} was achieved at an irradiation power of 1.5 W·cm^{-2} and the oxygen accumulation increased progressively over time. However, increasing the power density to 2.0 W·cm^{-2} did not yield a corresponding increase in oxygen production efficiency (Figs. S11(a) and S11(b) in the ESM). Based on these findings, an NIR power density of 1.5 W·cm^{-2} was selected for all subsequent experiments. Furthermore, to evaluate the oxygen generation performance of the Algae-UCNPs-robot under NIR excitation, a comparative analysis of oxygen production was conducted among different micro-nano systems in both PBS and mucin solutions (Figs. 3(b) and 3(c), and Fig. S12 in the ESM). The experimental results revealed that under NIR irradiation, the Algae-UCNPs-robot produced oxygen concentrations of 2.83 ± 0.25 mg·L^{-1} in PBS and 1.03 ± 0.06 mg·L^{-1} in mucin solution. These values represent 8.6-fold and 6.9-fold enhancements, respectively, compared to control groups without NIR irradiation. Notably, under identical conditions, the hybrid Algae-UCNPs-robot system exhibited superior performance, yielding 2.47 times and 1.74 times more oxygen in PBS and mucin solution, respectively, than the Algae + NIR group. Collectively, these results demonstrate that the Algae-UCNPs-robot possesses a remarkable and satisfactory oxygen production capacity when irradiated with NIR light at 1.5 W·cm^{-2}.

To further verify the intracellular oxygen-generation capability, we employed the hypoxia-sensitive fluorescent probe RDPP to assess cellular oxygenation levels [36]. Due to dynamic quenching, the presence of molecular oxygen can significantly reduce the fluorescence of RDPP anoxic probe. To establish a hypoxic model, A549 cells were first placed in an anaerobic bag for cultivation. Following RDPP staining and the addition of the microrobots, the intracellular oxygen levels were determined by measuring the RDPP fluorescence intensity using CLSM after 10 min of NIR irradiation (1.5 W·cm^{-2}). As shown in Fig. 3(d), intense red fluorescence was observed in the control, UCNPs + NIR, and Algae-UCNPs-robot + dark groups. In contrast, the Algae-UCNPs-robot + NIR group displayed nearly undetectable RDPP signals. Notably, the free Algae + NIR group failed to effectively quench the RDPP fluorescence, underscoring the pivotal role of the integrated Algae-UCNPs-robot system in achieving this oxygen-generating effect. These results collectively indicate that the Algae-UCNPs-robot possesses excellent oxygen-generation performance under NIR irradiation (Fig. 3(g)).

Subsequently, we assessed the expression of HIF-1α using immunofluorescence. HIF-1α is a key regulator that enables cellular and tissue adaptation to hypoxic conditions. Under hypoxic conditions, the degradation of HIF-1α is inhibited, leading to its accumulation and stabilization [37]. As shown in Fig. 3(e), following 10 min of NIR irradiation, a significant reduction in the green fluorescence intensity of HIF-1α was observed in the Algae-UCNPs-robot group. Although a slight reduction in fluorescence intensity was noted in the Algae + NIR group compared to the control, the Algae-UCNPs-robot + NIR treatment yielded a more substantial effect, attenuating HIF-1α expression by approximately 60% in hypoxic cells (Fig. 3(h)). A subsequent evaluation at the lung tissue level confirmed a similar trend in HIF-1α protein expression. Compared to the non-irradiated Algae-UCNPs-robot group, the Algae-UCNPs-robot + NIR group exhibited a marked attenuation in HIF-1α-associated green fluorescence (Fig. 3(f)). Quantitative analysis of fluorescence intensity demonstrated that the Algae-UCNPs-robot reduced HIF-1α expression by approximately 54% in lung tissue upon NIR irradiation, an effect significantly greater than the 24% reduction achieved by the Algae + NIR group (Fig. 3(i)). To further quantify these changes, we performed WB analysis of HIF-1α protein expression in hypoxic A549 cells (Fig. 3(j)). The results confirmed a significant downregulation of HIF-1α protein levels in the Algae-UCNPs-robot + NIR group compared to the Algae + NIR group (Fig. 3(k)). In summary, under NIR irradiation at 1.5 W·cm^{-2}, the Algae-UCNPs-robot generated substantial oxygen via photosynthesis, effectively alleviating hypoxic conditions in both cultured cells and lung tissues.

3.4 Lung retention and clearance

Atomization-based drug delivery enables direct targeting of the lungs and enhances drug bioavailability. To validate the feasibility of delivering the Algae-UCNPs-robot via atomization, we leveraged the autofluorescence of chlorophyll a in the microalgae and employed small animal *in vivo* imaging to track their distribution within the five-lobed lung tissue. As shown in Fig. S13(a) in the ESM, the motile microalgae robots demonstrated a more uniform distribution in mouse lungs post-nebulization compared to their static counterparts. Semi-quantitative fluorescence analysis further confirmed no significant difference in the overall fluorescence signals detected in the lungs (Fig. S13(b) in the ESM). We next measured the velocity of droplets containing the samples as they passed through the nebulizer. The results indicated that the motion speed of both bare algae and the microalgae robots remained largely unaffected by the atomization process, with no significant difference observed before and after nebulization (Fig. S14 and

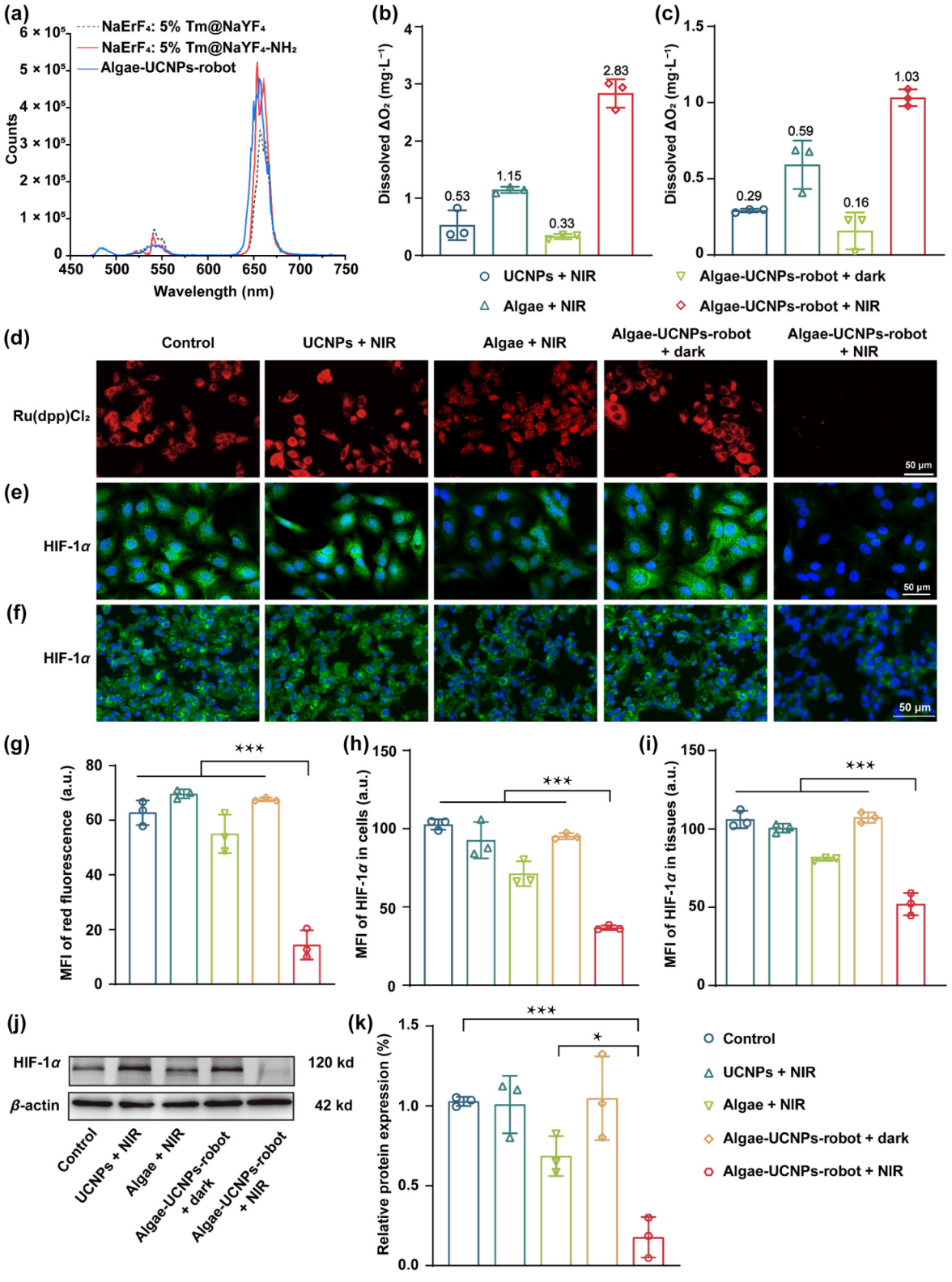

Figure 3 Oxygen production performance of Algae-UCNPs-robot. (a) Upconversion fluorescence spectra of UCNPs at different modification stages. (b) Oxygen production of Algae-UCNPs-robot in PBS buffer for 10 min (n = 3). (c) Oxygen production of Algae-UCNPs-robot in mucin solution for 10 min (n = 3). (d) Representative fluorescence image and (g) fluorescence quantification of anoxic cultured A549 cells (red) after being stained with RDPP anoxic probe and incubated with different micro-nano systems (n = 3). (e) Immunofluorescence staining image and (h) fluorescence quantification of HIF-1α protein (green fluorescence) after different micro-nano systems were incubated with hypoxic-treated A549 cells (n = 3). (f) Immunofluorescence staining image and (i) fluorescence quantification of HIF-1α protein (green fluorescence) in lung tissue after atomization with different micro and nano systems (n = 3). (j) WB analysis and (k) quantitative analysis of HIF-1α protein after different micro-nano systems were incubated with anoxic A549 cells (n = 3). Values are represented as means ± SD. One-way ANOVA (panels (g)–(i), and (k)) was used for statistical analysis. *P < 0.05, and ***P < 0.001.

Video S5 in the ESM). Subsequently, SYTOX Green staining was employed to assess the viability of Algae-UCNPs-robot before and after nebulization. The results presented in Fig. S15 in the ESM indicate that the viability was 96.17% before nebulization and 90.88% after nebulization. These findings demonstrate that the vast majority of cells (> 90%) remained viable following nebulization. Combined with motility analysis, the nebulization process did not significantly impair the motility and viability of the Algae-UCNPs-robot, confirming its feasibility as a delivery method for this system.

Following nebulization and inhalation, we investigated the pulmonary distribution of the Algae-UCNPs-robots. Leveraging the autofluorescence of chlorophyll a in the algae, lung tissues were harvested at various time points post-atomization for *ex vivo* fluorescence imaging to visualize the distribution. Non-motile UCNPs-modified *C. reinhardtii* (designated "Static-algae-UCNPs"), which were characterized by SEM (Fig. S16 in the ESM), served as a control. Under NIR irradiation, the Algae-UCNPs-robots had penetrated the entire lung tissue within 1 h and maintained strong fluorescence even at 24 h. In contrast, the signal from the Static-algae-UCNPs decreased sharply by 6 h and was nearly undetectable at 24 h (Fig. 4(a)). As shown in Fig. 4(b), the total fluorescence intensity of the motile Algae-UCNPs-robots gradually decreased over 48 h but remained consistently higher than that of the non-motile Static-algae-UCNPs group up to the 24-h time point. By 48 h, no significant difference in fluorescence intensity was observed between the two groups. In contrast, the Static-algae-UCNPs group exhibited a more rapid and pronounced signal reduction. Collectively, these data demonstrate that the inherent motility of the Algae-UCNPs-robots significantly enhances their retention within the lungs.

To further elucidate how active movement enhances pulmonary retention, we investigated the underlying clearance mechanism of the algae-based robots in the lungs. Macrophages are one of the primary resident immune cells in the lungs and play a key role in phagocytosing and clearing foreign particulates [38, 39]. Algae-UCNPs-robots and Static-algae-UCNPs were co-incubated with RAW264.7 macrophages at a 1:1 ratio. The culture supernatants were collected at various time intervals to measure the fluorescence intensity. As shown in Fig. 4(c), the residual fluorescence intensity in the supernatant for the Static-algae-UCNPs group was significantly lower than that of the Algae-UCNPs-robots group, indicating that Static-algae-UCNPs were more easily internalized by macrophages. The uptake of Algae-UCNPs-robots over time was quantified by calculating the number of unbound Algae-UCNPs-robots at different time points (Fig. S17(b) in the ESM). As shown in Fig. S17(a) in the ESM, the internalization rate of the Static-algae-UCNPs by macrophages was significantly faster compared to that of the motile Algae-UCNPs-robots. These results collectively indicate that the active movement of the Algae-UCNPs-robots facilitates their evasion of macrophage uptake.

To elucidate the *in vivo* clearance mechanism, we employed flow cytometry to analyze the uptake of the microrobots by macrophages at various time points following nebulization in mice (Fig. 4(d)). The uptake of Algae-UCNPs-robots by alveolar macrophages remained low within the first 6 h, with a relative increase observed at the 24-h time point. In contrast, approximately 30% of macrophages showed positive uptake of Static-algae-UCNPs at 6 h post-atomization, which was 2.5 times the uptake of Algae-UCNPs-robot (Fig. 4(e)). These findings confirm that alveolar macrophages represent the primary pathway for clearing algae-based particles from the lungs. The delayed phagocytosis of the Algae-UCNPs-robots observed *in vivo* is consistent with our *in vitro* results, providing a plausible explanation for their prolonged pulmonary retention.

To evaluate the biosafety of UCNPs and assess the risk of long-term accumulation that could lead to toxicity or organ burden, we investigated their *in vivo* metabolic profile. Quantitative analysis using inductively ICP-MS revealed a time-dependent decrease in the concentration of the Yttrium (Y) element (a component of UCNPs) in both lung tissue and blood. Compared to the level at 3 h post-nebulization, the Y element concentration in lung tissue dropped from 0.182 to 0.023 $\mu g \cdot g^{-1}$ by 48 h, constituting an 87.2% reduction. Correspondingly, the blood concentration decreased from 14.75 to 1.49 $\mu g \cdot L^{-1}$ over the same period, resulting in a clearance rate of 89.9% (Figs. 4(f) and 4(g)). In addition, fluorescence imaging of UCNPs in major mouse organs at various time points post-atomization showed a significant decrease in fluorescence signals across all examined organs at 48 h compared to 1 h (Fig. S18 in the ESM). These findings collectively indicate that the UCNPs can be effectively metabolized and cleared from the body over time, supporting their favorable biological safety profile.

3.5 Effect of Algae-UCNPs-robot on hypoxia in IPF mice

Subsequently, we evaluated the therapeutic efficacy of the Algae-UCNPs-robot in alleviating dyspnea in IPF model mice under NIR irradiation (980 nm, 1.5 $W \cdot cm^{-2}$). The IPF mouse model was first established via intratracheal instillation of BLM. Successful model establishment was confirmed by H&E staining after 7 days (Fig. S19 in the ESM). During the treatment period, a nebulization regimen was administered every two days. For the positive control group, SAL was nebulized once daily over a two-week period (Fig. 5(a)). As evidenced by the body weight change curve, IPF mice treated with Algae-UCNPs-robot plus NIR irradiation exhibited a significantly attenuated weight loss and maintained a better physiological status throughout the treatment course. These findings indicate the excellent *in vivo* biosafety of the Algae-UCNPs-robot (Fig. 5(b)).

For the therapeutic intervention, we employed an atomized drug delivery approach. One hour post-nebulization, the mice were subjected to NIR laser irradiation (980 nm, 1.5 $W \cdot cm^{-2}$). Subsequently, blood oxygen saturation (SpO_2) was measured using an oximeter. The temporal changes in murine SpO_2 are presented in Fig. 5(c). The model control group exhibited a significant decline in SpO_2 over the course of nebulization, indicative of the progressive physiological deterioration associated with IPF. Similarly, the SAL group failed to mitigate the SpO_2 decline, underscoring its limited therapeutic efficacy against IPF. In sharp contrast, the Algae-UCNPs-robot + NIR group displayed a substantially attenuated SpO_2 decline relative to other groups, maintaining a final level of 91.00% ± 2.24%. Conversely, the Static-algae-UCNPs + NIR group registered a significantly lower SpO_2 value of 86.00% ± 2.24%, with its overall performance being markedly inferior to that of the motile Algae-UCNPs-robot group. These results underscore the critical role of the microalgae robots' motility in achieving therapeutic outcomes. Collectively, the SpO_2 measurements demonstrate that under NIR irradiation, the oxygen generated by the photosynthesis of the nebulized microalgae robots within the lungs effectively alleviates the declining trend of blood oxygen saturation in IPF mice, thereby ameliorating their dyspnea symptoms.

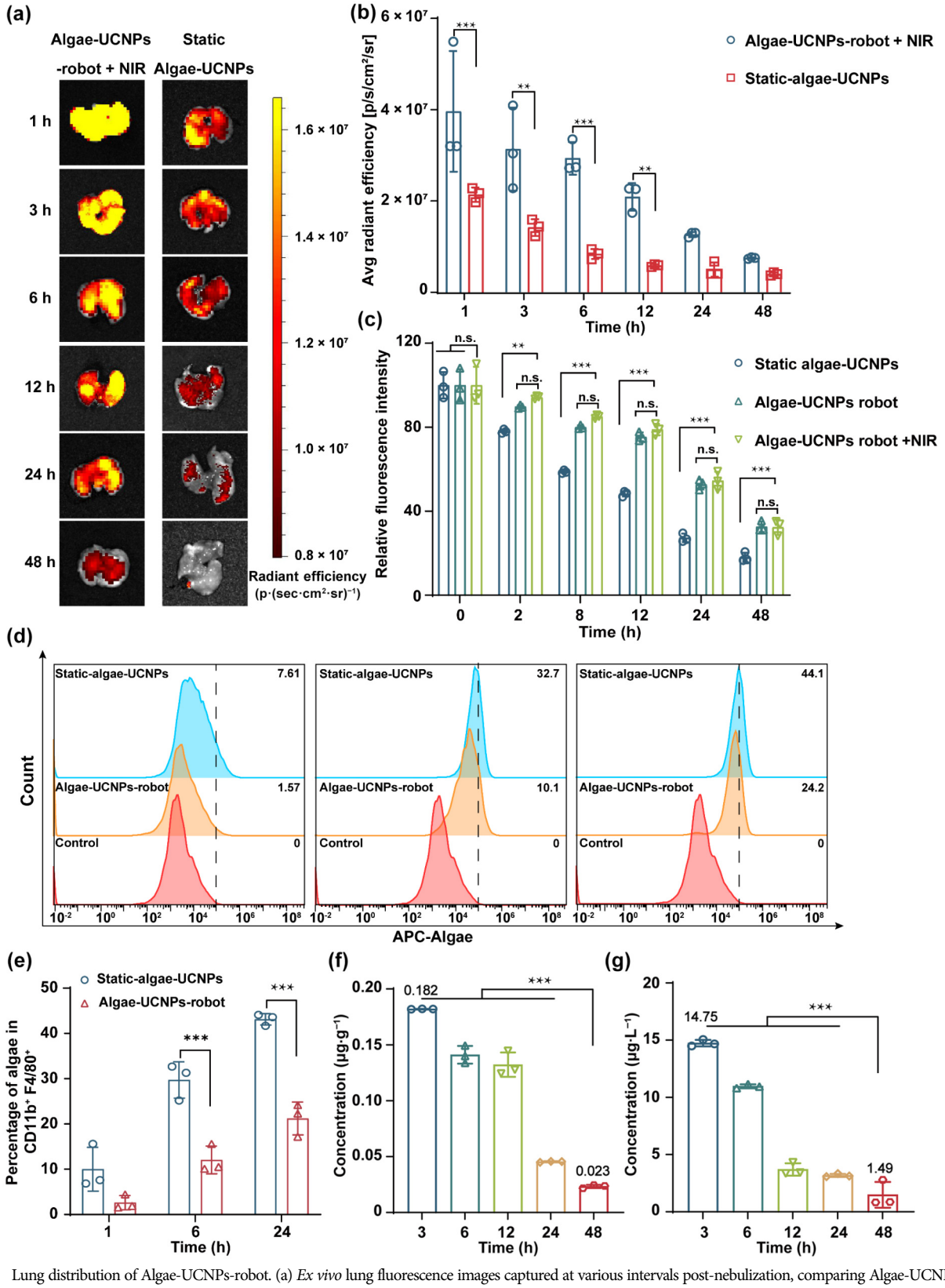

Figure 4 Lung distribution of Algae-UCNPs-robot. (a) *Ex vivo* lung fluorescence images captured at various intervals post-nebulization, comparing Algae-UCNPs-robot with Static-algae-UCNPs. (b) Fluorescence quantification in lung tissue at different time points (n = 3). (c) Fluorescence intensity variations of Algae-UCNPs-robot versus Static-algae-UCNPs, with/without NIR irradiation during macrophage co-culture (n = 3). (d) Flow cytometric analysis showing uptake of Algae-UCNPs-robot versus Static-algae-UCNPs by $CD11b^{+}F4/80^{+}$ alveolar macrophages after nebulization administration (n = 3). (e) Comparison of Algae-UCNPs-robot and Static-algae-UCNPs uptake by alveolar macrophages at different time points (n = 3). Changes of Y content in (f) lung tissue and (g) blood of IPF mice at different time points after atomizing microalgae robot (n = 3). Values are represented as means ± SD. Two-way ANOVA (panels (b), (c), and (e)) and One-way ANOVA (panels (f) and (g)) were used for statistical analysis. $^{*}P < 0.05$, $^{**}P < 0.01$, and $^{***}P < 0.001$. n.s. indicates no significant difference.

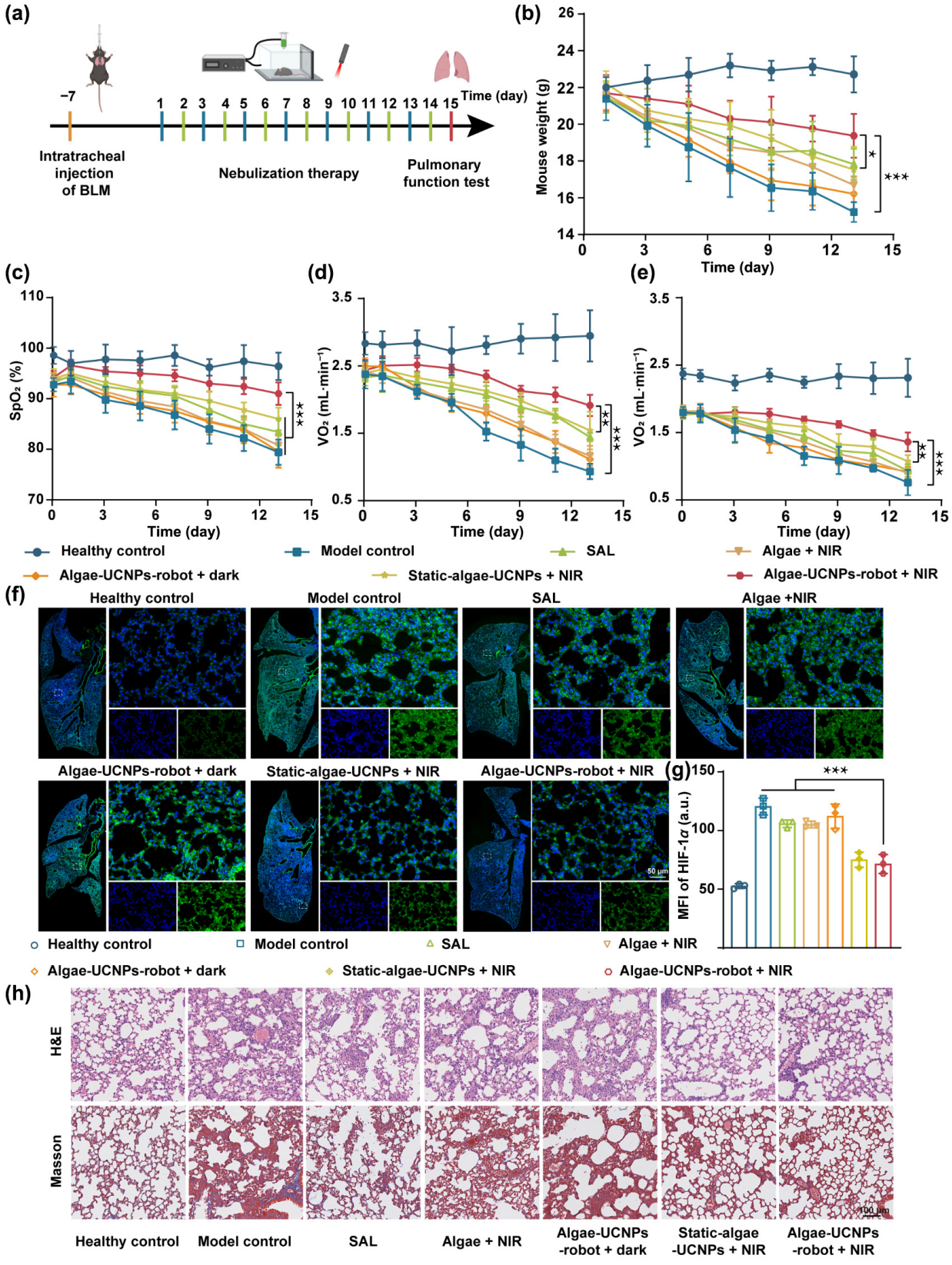

Figure 5 Effect of Algae-UCNPs-robot on hypoxia in IPF mice. (a) *In vivo* treatment timeline of IPF mice. (b) Body weight change curve of mice in each group (n = 5). (c) The variation curves of SpO_2 in each group of mice during atomization treatment (n = 5). (d) The variation curves of VO_2 in each group of mice over time during nebulization treatment (n = 5). (e) The variation curves of VCO_2 in each group of mice over time during nebulization treatment (n = 5). (f) Staining images of HIF-1α protein in lung tissue of mice in each group after treatment. (g) Average fluorescence quantification of HIF-1α protein (n = 3). (h) H&E and Masson staining images of lung tissues in each group of mice after nebulization treatment (scale bar: 100 μm). Values are represented as means ± SD. Two-way ANOVA (panels (b)–(e)) and One-way ANOVA (panel (g)) was used for statistical analysis. *P < 0.05, **P < 0.01, and ***P < 0.001.

In IPF mice, pathological features such as thickened alveolar walls and pulmonary fibrosis lead to a reduced area for gas exchange. This impairment results in diminished efficiency of CO_2 diffusion from the blood into the alveoli and consequently, a decrease in CO_2 excretion [40, 41]. Consequently, VCO_2 in IPF mice is significantly lower than that in healthy controls. Similarly, VO_2 is also typically subnormal, attributable to the compromised oxygen uptake capacity. To assess the severity of IPF and the therapeutic effect, mice were atomized and irradiated with NIR before being placed in a small animal respiratory metabolism detection system to monitor the changes of VCO_2 and VO_2 in mice. The results for these respiratory metabolic parameters (VCO_2 and VO_2) are presented in Figs. 5(d) and 5(e). As IPF progressed, the model control group exhibited a gradual decline in both VCO_2 and VO_2, reflecting the deterioration of respiratory metabolic function. In contrast, the Algae-UCNPs-robot + NIR group maintained significantly higher levels of VCO_2 and VO_2. This demonstrates that oxygen generated by the microalgae robots via photosynthesis effectively alleviated hypoxia and restored respiratory metabolic function in the IPF mice. Although the Static-algae-UCNPs + NIR group showed a moderate improvement, its effect was significantly less pronounced than that in the motile Algae-UCNPs-robot group. These findings further corroborate the superior dynamic oxygen production capacity afforded by the motility of the microalgae robots.

Following the treatment regimen, we assessed the expression of HIF-1α in lung tissues via immunofluorescence staining. The results showed that, compared with the BLM group, the green fluorescence intensity in the SAL group and the Algae + NIR group decreased to varying degrees. Notably, the Algae-UCNPs-robot + NIR group exhibited the most substantial decrease in HIF-1α fluorescence intensity. Moreover, the distribution of the residual green fluorescence in this group was considerably more uniform than that observed in the Static-algae-UCNPs + NIR group (Figs. 5(f) and 5(g)). This result indicated that the motion characteristics of microalgae robots played an important role in improving oxygen distribution. These findings demonstrate that the synergistic combination of dynamic oxygen production and autonomous motility in the microalgae robots potently enhances therapeutic outcomes by ensuring superior oxygen distribution, which effectively alleviates IPF-associated hypoxia.

The progression of pulmonary fibrosis severely compromises essential lung functions [42, 43]. To quantify these functional impairments, we employed whole-body plethysmography (WBP) following nebulization to analyze key lung function parameters across the different treatment groups. As shown in Fig. S20 in the ESM, the Algae-UCNPs-robot + NIR group exhibited significant reductions in inspiratory time, expiratory time, and inspiratory/expiratory pauses, alongside marked increases in respiratory rate, maximum inspiratory/expiratory flow, tidal volume, and mid-expiratory flow compared to the model control.

We further evaluated the extent of lung tissue injury and collagen deposition using H&E and Masson's trichrome staining, respectively. Histological analysis revealed severe alveolitis, extensive architectural damage, and near-complete loss of alveolar cavities in the SAL, Algae + NIR, and Algae-UCNPs-robot + dark groups. In contrast, lung tissues from the Static-algae-UCNPs + NIR and Algae-UCNPs-robot + NIR groups, while exhibiting modest neutrophilic infiltration and partial alveolar destruction, maintained a relatively preserved and orderly alveolar architecture (Fig. 5(h)). These findings indicate that while the Algae-UCNPs-robot + NIR treatment did not fully reverse established IPF, it effectively mitigated the decline in pulmonary function and alleviated pathological damage in the lung tissues of IPF mice.

We next investigated the *in vivo* biocompatibility of the microalgae-based robot following a two-week nebulization regimen. As summarized in Fig. S21 in the ESM, no significant alterations in hematological or serum biochemical parameters were observed in mice treated with Algae-UCNPs-robot alone or in combination with NIR, compared to the control group. Consistently, H&E staining of major organs revealed no detectable pathological abnormalities (Fig. S22 in the ESM). Regarding immune responses, enzyme-linked immunosorbent assay (ELISA) results showed that the levels of the IL-6 and the TNF-α in serum 48 h after inhalation administration were not clearly elevated compared with the control group (Fig. S23 in the ESM). These results confirm that the microalgae-based robotic system exhibited an excellent biosafety profile throughout the entire 14-day administration period. This favorable biocompatibility profile establishes a solid foundation for the potential translation of this microalgae robotic system for managing IPF-related respiratory distress.

4 Conclusions

Idiopathic pulmonary fibrosis is a chronic, progressive, and irreversible interstitial lung disease of unknown etiology, characterized primarily by pulmonary fibrosis and a gradual decline in lung function. Disease progression is invariably accompanied by severe hypoxemia and persistent dyspnea, profoundly compromising patients' quality of life. Current standard-of-care, including supplemental oxygen therapy, pulmonary rehabilitation, and anti-fibrotic/anti-inflammatory drugs, provides primarily symptomatic relief and is associated with considerable limitations. For instance, long-term high-concentration oxygen therapy carries a risk of oxygen toxicity, while the requisite equipment for continuous supplementation significantly impairs patient mobility and quality of life. Microalgae, as natural biomaterials, offer exceptional biosafety and the unique capability for spatiotemporally controllable, on-demand oxygen production *in vivo* via photosynthesis [44, 45]. However, the clinical translation of microalgae-based therapies is hampered by inherent challenges, including poor tissue penetration of visible light and their rapid clearance from the systemic circulation.

Inspired by the innate photosynthetic oxygen-generating capacity of microalgae [28, 30], we engineered a microrobotic platform by functionalizing *C. reinhardtii* with UCNPs. This platform, termed Algae-UCNPs-robot, is designed for targeted *in situ* oxygen production within the lungs in the context of IPF. The UCNPs can convert NIR laser light into red visible light, thereby inducing algae cells to perform photosynthesis and produce oxygen. *In vitro* assessments confirmed the platform's functionality, demonstrating that under NIR irradiation and with a UCNP concentration of 0.5 mg·mL^{-1}, the Algae-UCNPs-robot produced oxygen, resulting in an increase of 2.98 ± 0.05 mg·L^{-1} in the dissolved oxygen concentration. Notably, the platform retained its oxygen-producing capability even in a mucin-rich environment, yielding 1.03 ± 0.06 mg·L^{-1} of oxygen following 10 min of NIR exposure. Additionally, it significantly reduced the expression of HIF-1α in hypoxia-cultured cells and lung tissues, confirming its excellent oxygen generation performance. The therapeutic potential

of the Algae-UCNPs-robot was further validated *in vivo*. Notably, compared to the static control (Static-algae-UCNPs), the motile Algae-UCNPs-robot + NIR group facilitated more homogeneous oxygen distribution and exhibited a significantly prolonged retention time within the lung tissue, highlighting the importance of the microalgae robot's motility in improving oxygen delivery. In the IPF mouse model, treatment with Algae-UCNPs-robot + NIR group significantly attenuated the decline in SpO_2 and reduced HIF-1α protein expression.

In summary, this work successfully engineered a *Chlamydomonas reinhardtii*-based microrobotic platform via a facile click chemistry approach. This platform enabled effective NIR-triggered oxygen production and demonstrated significant efficacy in alleviating hypoxia in a murine model of IPF. The incorporated motility conferred enhanced evasion of pulmonary macrophage phagocytosis and promoted uniform intrapulmonary oxygen distribution, collectively contributing to an innovative therapeutic strategy for IPF. This research not only proposes a novel therapeutic avenue for IPF but also provides broader insights for the development of next-generation, active pulmonary delivery systems.

Electronic Supplementary Material: Supplementary material (algae-UCNPs-robot assembly, motion behavior, *in vitro* and *in vivo* hypoxia alleviation, lung retention, biosafety evaluations, supplementary videos) is available in the online version of this article at https://doi.org/10.26599/NR.2026.94908538.

Data availability

The original contributions presented in the study are included in the article and the Electronic Supplementary Materials, further inquiries can be directed to the corresponding author.

Acknowledgements

This work was supported by the National Natural Science Foundation of China (Nos. 82572424, 82473863, and 82222067), Natural Science Foundation of Henan Province (No. 252300421354), Scientific and Technological Innovation Talent in Central Plains, China Postdoctoral Science Foundation (No. 2023M743232), and the Postdoctoral Fellowship Program of CPSF (No. GZB20230676). We thank the members of Modern Analysis and Computing Center of Zhengzhou University for technical assistance.

Declaration of competing interest

The authors declare no conflict of interest.

Author contribution statement

H. L., K. G. Z., and M. Z. Y. performed experimental measurements. H. L., Q. X. Z., and F. Q. Z. drafted the paper. K. G. Z., X. J. Z., and Y. B. Y. revised the paper. W. G., N. Y., J. J. S., and Z.-H. W. contributed to the data interpretation and provided financial support.

Informed consent

Not applicable.

Ethics statement

All experimental procedures involving animals strictly abide by the Regulations on the Management of Experimental Animals of Zhengzhou University and have been approved by the Life Science Ethics Review Committee of the School of Pharmaceutical Sciences, Zhengzhou University (animal ethics code: yxy11sc20250012). C57 male mice (6–8 weeks) were purchased from Liaoning Changsheng Biotechnology Co. Ltd. (Ethics code: SCXK-2020-0001).

Use of AI statement

None.

References

[1] Lederer, D. J.; Martinez, F. J. Idiopathic pulmonary fibrosis. *N. Engl. J. Med.* **2018**, *378*, 1811–1823.
[2] Spagnolo, P.; Kropski, J. A.; Jones, M. G.; Lee, J. S.; Rossi, G.; Karampitsakos, T.; Maher, T. M.; Tzouvelekis, A.; Ryerson, C. J. Idiopathic pulmonary fibrosis: Disease mechanisms and drug development. *Pharmacol. Ther.* **2021**, *222*, 107798.
[3] Prasad, J.; Holland, A. E.; Glaspole, I.; Westall, G. Idiopathic pulmonary fibrosis: An Australian perspective. *Int. Med. J.* **2016**, *46*, 663–668.
[4] Hoffman, T. W.; van der Vis, J. J.; Biesma, D. H.; Grutters, J. C.; van Moorsel, C. H. M. Extrapulmonary manifestations of a telomere syndrome in patients with idiopathic pulmonary fibrosis are associated with decreased survival. *Respirology* **2022**, *27*, 959–965.
[5] Lynch III, J. P.; Huynh, R. H.; Fishbein, M. C.; Saggar, R.; Belperio, J. A.; Weigt, S. S. Idiopathic pulmonary fibrosis: Epidemiology, clinical features, prognosis, and management. *Semin. Respir. Crit. Care Med.* **2016**, *37*, 331–357.
[6] Zhou, A. Y.; Lang, Q.; Zhao, C. Y.; Mo, C. H. Nerandomilast shatters decade-long stalemate in fibrotic lung diseases: FDA fast track insights. *Inn. Med.* **2025**, *3*, 100151.
[7] Spagnolo, P.; Maher, T. M. A long and winding road: Drug development in idiopathic pulmonary fibrosis. *Am. J. Respir. Crit. Care Med.* **2024**, *209*, 1072–1073.
[8] Podolanczuk, A. J.; Thomson, C. C.; Remy-Jardin, M.; Richeldi, L.; Martinez, F. J.; Kolb, M.; Raghu, G. Idiopathic pulmonary fibrosis: State of the art for 2023. *Eur. Respir. J.* **2023**, *61*, 2200957.
[9] Glassberg, M. K.; Wijsenbeek, M. S.; Gilberg, F.; Petzinger, U.; Kirchgaessler, K. U.; Albera, C. Effect of pirfenidone on breathlessness in patients with idiopathic pulmonary fibrosis. *Eur. Respir. J.* **2019**, *54*, 1900399.
[10] Reinaldo, G. P.; Araújo, C. L. P.; Schneider, B.; Florian, J.; Machado, S. C.; Hochhegger, B.; Dal Lago, P. Validity and reliability of the Glittre-ADL test in individuals with idiopathic pulmonary fibrosis. *Physiother. Theory Pract.* **2022**, *40*, 1101–1109.
[11] O'Donnell, D. E.; Neder, J. A.; Harle, I.; Moran-Mendoza, O. Chronic breathlessness in patients with idiopathic pulmonary fibrosis: A major challenge for caregivers. *Expert Rev. Respir. Med.* **2016**, *10*, 1295–1303.
[12] Oruç, M.; Esen, B.; Taylan, M.; Nergis, Y.; Sahin, A. The role of duration of hyperbaric oxygen therapy on lung injury: An experimental study lung injury and hyperbaric oxygen therapy. *Turk. Thorac. J.* **2018**, *19*, 61–65.
[13] Jacobs, S. S.; Lederer, D. J.; Garvey, C. M.; Hernandez, C.; Lindell, K. O.; McLaughlin, S.; Schneidman, A. M.; Casaburi, R.; Chang, V.; Cosgrove, G. P. et al. Optimizing home oxygen therapy. *An official american thoracic society workshop report. Ann. Am. Thorac. Soc.* **2018**, *15*, 1369–1381.
[14] Ortega, M. A.; Fraile-Martinez, O.; García-Montero, C.; Callejón-Peláez, E.; Sáez, M. A.; Álvarez-Mon, M. A.; García-Honduvilla, N.; Monserrat, J.; Álvarez-Mon, M.; Bujan, J. et al. A general overview

on the hyperbaric oxygen therapy: Applications, mechanisms and translational opportunities. *Medicina* **2021**, *57*, 864.
[15] Xin, Y. T.; Yu, Y. J.; Su, M. H.; Li, X. H.; Elsabahy, M.; Gao, H. *In situ*-activated photothermal nanoplatform for on-demand NO gas delivery and enhanced colorectal cancer treatment. *J. Controlled Release* **2023**, *359*, 69–84.
[16] Voelker, M. T.; Laudi, S.; Henkelmann, J.; Bercker, S. Extracorporeal membrane oxygenation and perfluorocarbon in a therapy refractory case of acute respiratory distress syndrome. *Ann. Thorac. Surg.* **2022**, *113*, e355–e358.
[17] Wang, H. R.; Guo, Y. F.; Wang, C.; Jiang, X.; Liu, H. H.; Yuan, A. H.; Yan, J.; Hu, Y. Q.; Wu, J. H. Light-controlled oxygen production and collection for sustainable photodynamic therapy in tumor hypoxia. *Biomaterials* **2021**, *269*, 120621.
[18] Jiang, L. Y.; Bai, H. T.; Liu, L. B.; Lv, F. T.; Ren, X. Q.; Wang, S. Luminescent, oxygen-supplying, hemoglobin-linked conjugated polymer nanoparticles for photodynamic therapy. *Angew. Chem., Int. Ed.* **2019**, *58*, 10660–10665.
[19] Kim, H.; Yoon, J.; Kim, H. K.; Lee, W. T.; Nguyen, N. T.; Le, X. T.; Lee, E. H.; Lee, E. S.; Oh, K. T.; Choi, H. G. et al. Upconverting nanoparticle-containing erythrocyte-sized hemoglobin microgels that generate heat, oxygen and reactive oxygen species for suppressing hypoxic tumors. *Bioact. Mater.* **2023**, *22*, 112–126.
[20] Yang, Z. W.; Shi, C. S.; Cheng, D. L.; Wang, Y.; Xing, Y.; Du, F. F.; Wu, F. F.; Jin, Y.; Dong, Y. L.; Li, M. L. Biomimetic nanomaterial-facilitated oxygen generation strategies for enhancing tumour treatment outcomes. *Front. Bioeng. Biotechnol.* **2022**, *10*, 1007960.
[21] Ghaffari-Bohlouli, P.; Jafari, H.; Okoro, O. V.; Alimoradi, H.; Nie, L.; Jiang, G. H.; Kakkar, A.; Shavandi, A. Gas therapy: Generating, delivery, and biomedical applications. *Small Methods* **2024**, *8*, 2301349.
[22] Chen, M. X.; Xu, T. Y.; Song, L. L.; Sun, T.; Xu, Z. H.; Zhao, Y. J.; Du, P. X.; Xiong, L.; Yang, Z. K.; Jing, J. et al. Nanotechnology based gas delivery system: A “green” strategy for cancer diagnosis and treatment. *Theranostics* **2024**, *14*, 5461–5491.
[23] Wijffels, R. H.; Barbosa, M. J. An outlook on microalgal biofuels. *Science* **2010**, *329*, 796–799.
[24] Ehrenfeld, C.; Veloso-Giménez, V.; Corrales-Orovio, R.; Rebolledo, R.; Boric, M. P.; Egaña, J. T. Microalgae share key features with human erythrocytes and can safely circulate through the vascular system in mice. *Appl. Microbiol. Biotechnol.* **2023**, *107*, 4621–4633.
[25] Fu, Y. H.; Xie, X. S.; Wang, Y. F.; Liu, J.; Zheng, Z. Z.; Kaplan, D. L.; Wang, X. Q. Sustained photosynthesis and oxygen generation of microalgae-embedded silk fibroin hydrogels. *ACS Biomater. Sci. Eng.* **2021**, *7*, 2734–2744.
[26] Qiao, Y.; Yang, F.; Xie, T. T.; Du, Z.; Zhong, D. N.; Qi, Y. C.; Li, Y. Y.; Li, W. L.; Lu, Z. M.; Rao, J. H. et al. Engineered algae: A novel oxygen-generating system for effective treatment of hypoxic cancer. *Sci. Adv.* **2020**, *6*, eaba5996.
[27] Clement, M.; Daniel, G.; Trelles, M. Optimising the design of a broad-band light source for the treatment of skin. *J. Cosmet. Laser Ther.* **2005**, *7*, 177–189.
[28] Huo, M. F.; Liu, P. L.; Zhang, L. L.; Wei, C. Y.; Wang, L. Y.; Chen, Y.; Shi, J. L. Upconversion nanoparticles hybridized cyanobacterial cells for near-infrared mediated photosynthesis and enhanced photodynamic therapy. *Adv. Funct. Mater.* **2021**, *31*, 2010196.
[29] Zhang, Y. H.; Liu, H. F.; Dai, X. Y.; Li, H.; Zhou, X. H.; Chen, S. Z.; Zhang, J. C.; Liang, X. J.; Li, Z. H. Cyanobacteria-based near-infrared light-excited self-supplying oxygen system for enhanced photodynamic therapy of hypoxic tumors. *Nano Res.* **2021**, *14*, 667–673.
[30] Simon, J.; Kósa, A.; Bóka, K.; Vági, P.; Simon-Sarkadi, L.; Mednyánszky, Z.; Horváth, Á. N.; Nyitrai, P.; Böddi, B.; Preininger, É. Self-supporting artificial system of the green alga *Chlamydomonas reinhardtii* and the ascomycetous fungus *Alternaria infectoria*. *Symbiosis* **2017**, *71*, 199–209.
[31] Zhang, F. Y.; Li, Z. X.; Duan, Y. O.; Abbas, A.; Mundaca-Uribe, R.; Yin, L.; Luan, H.; Gao, W. W.; Fang, R. H.; Zhang, L. F. et al. Gastrointestinal tract drug delivery using algae motors embedded in a degradable capsule. *Sci. Robot.* **2022**, *7*, eabo4160.
[32] Yasa, O.; Erkoc, P.; Alapan, Y.; Sitti, M. Microalga-powered microswimmers toward active cargo delivery. *Adv. Mater.* **2018**, *30*, 1804130.
[33] Zhang, F. Y.; Zhuang, J.; Li, Z. X.; Gong, H.; de Ávila, B. E. F.; Duan, Y. O.; Zhang, Q. Z.; Zhou, J. R.; Yin, L.; Karshalev, E. et al. Nanoparticle-modified microrobots for *in vivo* antibiotic delivery to treat acute bacterial pneumonia. *Nat. Mater.* **2022**, *21*, 1324–1332.
[34] Zhang, F. Y.; Guo, Z. Y.; Li, Z. X.; Luan, H.; Yu, Y. Y.; Zhu, A. T.; Ding, S. C.; Gao, W. W.; Fang, R. H.; Zhang, L. F. et al. Biohybrid microrobots locally and actively deliver drug-loaded nanoparticles to inhibit the progression of lung metastasis. *Sci. Adv.* **2024**, *10*, eadn6157.
[35] Bian, W. J.; Lin, Y.; Wang, T.; Yu, X.; Qiu, J. B.; Zhou, M.; Luo, H. M.; Yu, S. F.; Xu, X. H. Direct identification of surface defects and their influence on the optical characteristics of upconversion nanoparticles. *ACS Nano* **2018**, *12*, 3623–3628.
[36] Yang, Z. L.; Wen, J.; Wang, Q.; Li, Y. J.; Zhao, Y.; Tian, Y.; Wang, X. F.; Cao, X. F.; Zhang, Y. L.; Lu, G. M. et al. Sensitive, real-time, and *in-vivo* oxygen monitoring for photodynamic therapy by multifunctional mesoporous nanosensors. *ACS Appl. Mater. Interfaces* **2019**, *11*, 187–194.
[37] Liu, Y.; Gu, Y. J.; Ng, S.; Deng, Z. A.; Lyon, C. J.; Koay, E. J.; Ning, B.; Katz, M. H.; Chiao, P. J.; Fan, J. et al. Circulating levels of hydroxylated bradykinin function as an indicator of tissue HIF-1α expression. *Sci. Bull.* **2020**, *65*, 1570–1579.
[38] Liu, X. S.; Xie, X. D.; Jiang, J. H.; Lin, M.; Zheng, E.; Qiu, W.; Yeung, I.; Zhu, M. T.; Li, Q. L.; Xia, T. et al. Use of nanoformulation to target macrophages for disease treatment. *Adv. Funct. Mater.* **2021**, *31*, 2104487.
[39] Huang, P. K.; Wei, S. S.; Huang, W. H.; Wu, P. H.; Chen, S. Y.; Tao, A. L.; Wang, H. Y.; Liang, Z. Y.; Chen, R. C.; Yan, J. et al. Hydrogen gas inhalation enhances alveolar macrophage phagocytosis in an ovalbumin-induced asthma model. *Int. Immunopharmacol.* **2019**, *74*, 105646.
[40] Wu, H. J.; Yu, Y. Y.; Huang, H. W.; Hu, Y. C.; Fu, S. L.; Wang, Z.; Shi, M. T.; Zhao, X.; Yuan, J.; Li, J. et al. Progressive pulmonary fibrosis is caused by elevated mechanical tension on alveolar stem cells. *Cell* **2020**, *180*, 107–121.e17.
[41] Amariei, D. E.; Dodia, N.; Deepak, J.; Hines, S. E.; Galvin, J. R.; Atamas, S. P.; Todd, N. W. Combined pulmonary fibrosis and emphysema: Pulmonary function testing and a pathophysiology perspective. *Medicina* **2019**, *55*, 580.
[42] Nokes, B.; Afshar, K. Adjunctive therapies in idiopathic pulmonary fibrosis—where do we stand. *J. Thorac. Dis.* **2019**, *11*, 357–360.
[43] Li, X. N.; Lin, Y. P.; Han, M. M.; Fang, Y. F.; Xing, L.; Jeong, J. H.; Jiang, H. L. Modulating fibrotic mechanical microenvironment for idiopathic pulmonary fibrosis therapy. *Adv. Mater.* **2024**, *36*, 2407661.
[44] Yin, S. Y.; Jin, W. B.; Xi, T. T.; Zhou, X.; He, Z. Q.; Meng, X. L.; Naushad, M.; Jiang, G. M.; Li, X. Factors affect the oxygen production of *Chlorella pyrenoidosa* in a bacterial-algal symbiotic system: Light intensity, temperature, pH and static magnetic field. *Process Saf. Environ. Protect.* **2024**, *184*, 492–501.
[45] Day, A. G.; Brinkmann, D.; Franklin, S.; Espina, K.; Rudenko, G.; Roberts, A.; Howse, K. S. Safety evaluation of a high-lipid algal biomass from *Chlorella protothecoides*. *Regul. Toxicol. Pharm* **2009**, *55*, 166–180.